



Impact of flow rates and electrode specifications on degradations during repeated startups and shutdowns in polymer-electrolyte membrane fuel cells



J. Dillet ^{a,b}, D. Spernjak ^c, A. Lamibrac ^{a,b}, G. Maranzana ^{a,b,*}, R. Mukundan ^c, J. Fairweather ^c, S. Didierjean ^{a,b}, R.L. Borup ^c, O. Lottin ^{a,b}

^a LEMTA, Université de Lorraine, 2, Avenue de la forêt de Haye, B.P. 160, 54504 Vandoeuvre-lès-Nancy, France

^b LEMTA, CNRS, Vandoeuvre-lès-Nancy, France

^c Los Alamos National Laboratory, Los Alamos, NM, USA

HIGHLIGHTS

- To distinguish between the effects of startup and shutdown on performance degradation.
- The internal currents during SU and SD operation are measured in a segmented cell.
- Cells with different membrane-electrode assemblies are subjected to SU or SD sequences.
- Influence of the cathode and anode Pt loading, and the type of carbon for cathode catalyst support.

ARTICLE INFO

Article history:

Received 17 September 2013

Received in revised form

24 October 2013

Accepted 29 October 2013

Available online 10 November 2013

Keywords:

Segmented PEM fuel cell

Corrosion of carbon support

Catalyst layer

Spatially resolved degradation

Startup and shutdown

ABSTRACT

Separate testing protocols for fuel cell startup (SU) and shutdown (SD) are developed to distinguish between the effects of SU and SD on performance degradation. The internal currents during SU and SD operation are measured in a segmented cell to evaluate the charge exchanged between the active (H_2/Air) and passive (Air/Air) portions of the cell. Cells with different membrane-electrode assemblies (MEAs) are subjected to SU or SD sequences to evaluate the time evolution of spatially resolved decrease of performance and electrochemical active surface area (ECSA). We examine the influence of the cathode and anode Pt loading, and the type of carbon for cathode catalyst support.

Both the CO_2 emissions and the charges exchanged increase with the common residence time of air and hydrogen in the anode compartment. However, the evolved CO_2 accounts for less than 25% of the total exchanged charge. Startups are consistently more damaging than the shutdowns, evidenced by more evolved CO_2 and charge exchanged, severe ECSA decrease, and higher performance losses.

© 2013 Elsevier B.V. All rights reserved.

1. Introduction

Despite recent efforts in PEM fuel cell research and development, sufficient lifetimes for transportation and stationary applications have not yet been achieved within satisfactory cost and performance targets. Fuel cell degradation mechanisms can affect the membrane, the electrodes, the gas diffusion layers (GDLs), the bipolar plates and even the gaskets. Although all these mechanisms are not fully understood, some of the operating conditions that

accelerate the degradation of Membrane-Electrode Assemblies (MEAs) are well known [1–5]. Among them, startups and shutdowns (SU/SD) can be extremely harmful to the stability of the PEMFC components, especially the cathode electrode. Compared to the normal (or, steady state) fuel cell operation, SU/SD transients lead to higher rates of electrochemical oxidation of the carbon supporting the cathode Pt catalyst, mainly because of the simultaneous presence of oxygen (air) and hydrogen in the anode compartment [6]. The presence of air in the anode compartment can be avoided or delayed during shutdowns (for instance by closing the inlet and the outlet of the anode compartment to maintain a homogenous concentration while hydrogen slowly permeates through the membrane). Various mitigation strategies have been developed which can limit the degradation due to SU/SD

* Corresponding author. LEMTA, Université de Lorraine, 2, Avenue de la forêt de Haye, B.P. 160, 54504 Vandoeuvre-lès-Nancy, France.

E-mail address: Gael.Maranzana@univ-lorraine.fr (G. Maranzana).

operation, however, such mitigation strategies can cause other durability issues and they are challenging to implement, especially when the fuel cell has been stopped for a long time [7,8]. For a review on various mitigation strategies from the patent literature see ref 8 and references within Ref. [8].

When the anode compartment is divided into a part already (still) filled with hydrogen and another part where air is still (already) present, startups (shutdowns) lead to the occurrence of internal currents flowing between the active region (H_2/air) and the passive region (air/air) of the cell. The active portion (top region in Fig. 1a) operates normally (i.e. as a H_2/air fuel cell), with oxygen reduction at the cathode and hydrogen oxidation at the anode (marked in red in Fig. 1). (For interpretation of the references to color in this figure, the reader is referred to the web version of this article.) The reverse currents appear in the passive part, i.e. the part which is not yet supplied with hydrogen (bottom region in Fig. 1a). These reverse currents can be measured using segmented cells [9–13]. Although they can be, in a very general manner, considered as fuel starvation events, the exact nature of reverse currents is not yet well understood. One of the first interpretations was proposed by Reiser et al. [6] who associated them with high cathode potential excursions, leading to accelerated carbon oxidation of cathode catalyst support [14]. Indeed, the occurrence of carbon corrosion was confirmed by various studies, through the measurement of CO_2 emissions at the cathode exhaust [1–5,15,16] and via post-mortem analyses of aged MEA [1,3,4,17,18]. Furthermore, the post-mortem analyses and the local measurement of CO_2 emissions along the cathode channel [19], ECSA, and performance [8] by various research groups indicate that carbon corrosion occurs heterogeneously over the MEA active surface: carbon corrosion in the cathode catalyst layer (CL) is accelerated in the region of the reverse current flow, and is mainly governed by the common residence time of air and hydrogen in the anode compartment [9,20,21].

In previous works, we proposed that the reverse currents can be decomposed into capacitive and faradic contributions [9,11]. Recent results [10] indicated that the charge corresponding to CO_2 emissions stands for only a few tenths of the faradic contribution. Consequently, around 80% of the reverse current is driven by phenomena other than complete carbon oxidation, such as reversible or irreversible catalyst oxidation, partial carbon oxidation, and water splitting. One of the objectives of the present work is to delineate the contribution of carbon oxidation to the charge measured from the internal currents. The internal currents during SU and SD operation were measured in a segmented cell to evaluate the charge exchanged between the active and passive portions of

the cell. Carbon corrosion was quantified by measuring the CO_2 emissions at the cathode exhaust. Separate testing protocols for startup (SU) and shutdown (SD) were developed, and are used to distinguish between the effects of SU and SD on performance degradation along the cell area. Cells with several different MEA materials were subjected to a series of SU or SD tests to explore the influence of anode and cathode Pt loading, cathode carbon support and gas flow rates. For this, we studied the time evolution of CO_2 emissions at the cathode exhaust, spatially resolved performance, and Pt Electro Chemical Surface Area (ECSA).

2. Experimental work

2.1. Segmented fuel cell design

This work was performed using a segmented cell with an active area of $1\text{ cm} \times 30\text{ cm}$, described in Ref. [9] and shown in Fig. 2. Flow field on both cathode and anode consists of five parallel channels, 30 cm long. Channel dimensions are 0.7 mm in depth $\times 1\text{ mm}$ in width on the cathode and $0.5\text{ mm} \times 1\text{ mm}$ on the anode. Lands are 1 mm wide. The cathode compartment was machined in a brass plate, which was then segmented and gold plated. The current was collected independently from 20 electrically insulated segments along the channel length. PTFE sheets ($50\text{ }\mu\text{m}$ thick) were inserted between the adjacent segments to ensure electrical insulation. The anode flow-field plate was machined in a non-segmented brass block which was then gold plated.

Hydrogen and air flow in opposite directions (counter-flow) in the anode and cathode compartments. The cathode segments are numbered from 1 to 20 in the direction of the air flow during normal fuel cell operation (segment #1 = air inlet/ H_2 outlet, segment #20 = air outlet/ H_2 inlet), as shown in Fig. 2. During shutdown operation, the air is injected through the hydrogen inlet on the anode side. The cell temperature was controlled using a cooling circuit (coolant channels in both end-plates) and a thermostatic bath. The fuel cell was operated at $80\text{ }^\circ\text{C}$ and atmospheric pressure (i.e. zero backpressure). Humidity of all inlet gases was held constant, at 90% RH.

2.2. MEA materials

Membrane-electrode assemblies (MEAs) were fabricated by Ion Power Inc., using Pt/C catalysts from Tanaka Kikinzoku Kogyo K.K. Four different MEAs were tested (Table 1): the reference MEA had cathode/anode Pt loadings of $0.2/0.08\text{ mg}_{\text{Pt}}/\text{cm}^2$ the cathode and

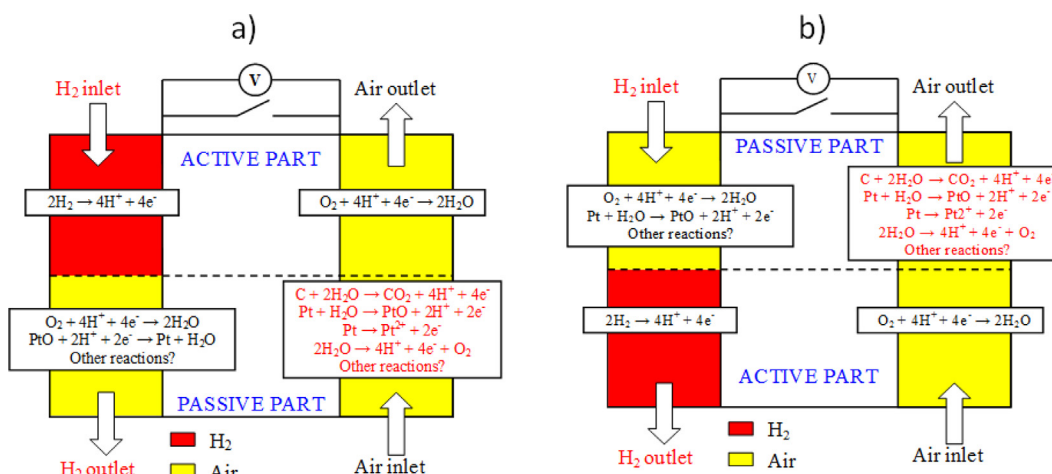


Fig. 1. Schematic of reverse currents and possible electrochemical reactions occurring in the passive part of the cell during startup (a) and shutdown (b).



Fig. 2. Segmented fuel cell with five long parallel channels. The arrows show the flow direction during normal fuel cell operation. The coolant circuit used to control the cell temperature flows through the aluminum end-plate (under the gold plated flow field).

anode material references were TEC 10V40E ($\text{Pt/C} = 40\%$) and TEC 10V20E ($\text{Pt/C} = 20\%$), respectively, with Vulcan XC72 carbon as the catalyst support in both cases ($240 \text{ m}^2/\text{g}$ specific surface area). In the second and third MEA types, Pt loading (i.e. the electrode thickness) was increased on the cathode and on the anode, respectively; the cathode and anode materials remained almost identical to those of the reference MEA. With the fourth MEA type, the effect of the cathode catalyst support is examined by using carbon with a higher specific surface area (TEC 10E40E; $\text{Pt/C} = 40\%$) with $800 \text{ m}^2/\text{g}$ amorphous carbon. The proton-exchange-membrane was the same in all experiments: XL membrane by DuPont™ (25 μm thick). The same GDL material was used in all tests, on both cathode and anode: SGL24BC by SGL Carbon – 240 μm thick, compressed to 200 μm using fuel cell hardware and Teflon gaskets. The MEAs and GDLs were not segmented.

2.3. In situ fuel cell characterization

In situ characterization was performed at the beginning of life (BoL) and periodically during SU and SD series. We recorded polarization curves for both the entire cell and individual segments along the cell, cell voltage during steady-state operation at constant current (0.67 A cm^{-2}), and ECSA. During startups, shutdowns, and normal steady-state fuel cell operation, the local current could reach up to 1.5 A per segment: these local currents were measured by 20 shunt resistors of $5 \text{ m}\Omega$ each and recorded by a data processing and acquisition system at a maximum frequency of 10 kHz. When voltammograms were recorded, the maximum current densities were on the order of 30 mA/segment, measured using Hall current sensors (CT 0.1-P – LEM with a range of $\pm 200 \text{ mA}$).

All MEAs were first conditioned by repeating the following sequence for 50 times: operation at 0.6 V for 45 s, open circuit for

30 s, and operation at 0.3 V for 60 s. Voltammetry was used to estimate the platinum ECSA and the hydrogen permeation through the membrane. The permeation measurements were performed at 0.6 V over 20 s with hydrogen at the anode and nitrogen at the cathode: the corresponding current densities were between 1.3 mA cm^{-2} and 1.6 mA cm^{-2} (Section 5). The cathode ECSA for all MEA materials ranged between 48 and $58 \text{ m}^2/\text{g}_{\text{Pt}}$ (Table 1). These values were obtained by cycling the potential between 0.1 and 1.2 V at a sweep rate of 50 mV s^{-1} . The ECSA values in Table 1 were calculated using the platinum loading value measured by XRF.

Characterization during each SU and SD included measurements of voltage, internal currents, and CO_2 evolution. To ensure accurate measurement of the evolved CO_2 on the cathode side, the air feeding the fuel cell was filtered using soda lime to eliminate carbon dioxide at the inlet. In addition, the cathode exhaust gases were thoroughly dehydrated using a condenser and a home-made Nafion® membrane dryer, as the CO_2 measurement is sensitive to water in the gas stream. This enabled the measurement of CO_2 emissions during both steady-state and transient fuel-cell operation using a single beam Infrared Multi-Component Analyzer (600 series by California Analytical Instruments, Inc.). The CO_2 measurement setup was carefully calibrated using a CO_2 -free gas and a 500 ppm CO_2/N_2 reference mixture. We confirmed that the water knockout process did not affect the measured CO_2 concentration.

3. Influence of flow rates and MEA materials on charge exchanged and CO_2 emissions during individual startups/shutdowns

The fresh MEAs were first characterized by performing individual startups and shutdowns at open circuit: hydrogen was injected in the air-filled anode compartment at startup and air was injected in the hydrogen-filled anode compartment at shutdown. The inlet flow rates of hydrogen and air were varied between 1 and 90 slph (standard liters per hour), which corresponds to average gas velocities in the channels comprised between 0.1 and 10 m s^{-1} and common residence times of air and hydrogen in the anode compartment between 3 and 0.03 s. These values were determined experimentally from the shift in the direction of the internal currents during individual startups or shutdowns. It must be kept in mind that the theoretical velocities estimated starting from the channels cross-section and gas injection flow rates are much higher because (i) the flow through the GDL is significant and (ii) hydrogen consumption slows down the hydrogen/air front [21]. The experiments were done by scanning the flow rates from high (least damage) to low flow rate (most damaging to the MEA).

While injecting hydrogen at startup (or air at shutdown), the anode compartment of the cell is temporarily divided into an active (i.e. hydrogen-rich) region and a passive (hydrogen-starved) region. As a consequence, the active region of the cell (Air/Hydrogen) drives the reverse currents in the passive region (Air/Air). Fig. 3

Table 1
MEA materials. The anode carbon support was Vulcan XC72 in all cases.

MEA	Reference MEA	Higher cathode Pt loading	Higher anode Pt loading	Higher carbon specific surface
Cathode Pt loading (as measured by XRF) ($\text{mg}_{\text{Pt}}/\text{cm}^2$)	0.27	0.61	0.31	0.24
Cathode Pt loading (planned) ($\text{mg}_{\text{Pt}}/\text{cm}^2$)	0.2	0.44	0.2	0.2
Cathode carbon support	Vulcan XC72 240 m^2/g	Vulcan XC72 240 m^2/g	Vulcan XC72 240 m^2/g	Amorphous carbon 800 m^2/g
Cathode ECSA at BoL ($\text{m}^2/\text{g}_{\text{Pt}}$)	48	45	55	58
Anode Pt loading (as measured by XRF) ($\text{mg}_{\text{Pt}}/\text{cm}^2$)	0.09	0.09	0.18	0.09
Anode Pt loading (planned) ($\text{mg}_{\text{Pt}}/\text{cm}^2$)	0.1	0.1	0.2	0.1

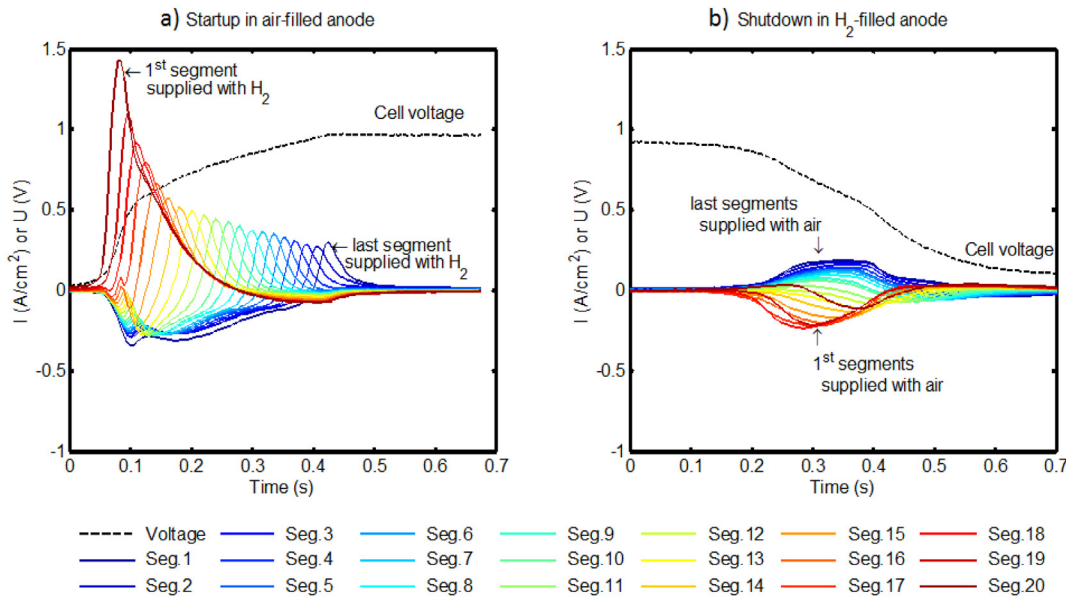


Fig. 3. Time evolution of local current densities in individual segments (solid colored lines) and cell voltage (dotted black line). Air was introduced through the hydrogen inlet (segment #20) at shutdown. (a) Startup with 10 slph of H₂ introduced in the air-filled anode. (b) Shutdown with 10 slph of air introduced in the H₂-filled anode.

illustrates the internal currents (vs. time) measured with the reference MEA during fuel cell SU (SD) when 10 slph of hydrogen (air) is injected in the anode compartment previously filled with air (hydrogen). For the average gas velocity in the channels of 1 m s^{-1} , the common residence time of air and hydrogen in the anode compartment is of about 0.3 s. During a startup (Fig. 3a), the forward (or, positive) currents can reach values as high as 1.5 A cm^{-2} in the first segment fed with hydrogen during startup (H₂ inlet, segment #20, Fig. 2). The reverse (or, negative) currents are smaller overall, while their maximum absolute value approaches 0.5 A cm^{-2} in the last segment fed with hydrogen (H₂ outlet, segment #1, Fig. 2). The maximum absolute values of both the forward and reverse currents are lower during shutdowns than during startups. Consequently, the total charge exchanged between the active and passive parts of the cell (i.e. the integral over time and space of the reverse currents divided by the cell active area [9]) is lower during the shutdown (0.02 C cm^{-2}) than during the startup (0.03 C cm^{-2}). The current density patterns are also different from those observed during startup. The results presented in the following paragraphs show that the charge exchanged (Fig. 4) and CO₂ emissions (Fig. 5) were lower during SD than during SU and that startups were more damaging (Section 4), regardless of the catalyst loading on anode and cathode, or carbon support specific surface area at the cathode. In addition, in situ measurements of local potential [21] show that the cathode reaches higher potential during startups than during shutdowns. However, it must be mentioned that there is no consensus in the literature regarding the relative impact of SU and SD in term of carbon corrosion [16,17,22–25]. Higher degradations during shutdowns were recorded with short [22] or relatively long air residence time [24,25]. There are several points to note regarding this.

- The possibility of Pt oxidation in the passive part of the anode compartment once air is introduced limits the oxygen concentration in the anode catalyst layer, the reverse currents, and thus the rate of the carbon support oxidation in the passive part of the cathode compartment [26]. Pt oxidation does not occur to the same extent at startup because the anode compartment is initially filled with air and the surface coverage of the oxide on

catalyst particles much higher. In this regards, equal gas residence times should yield lower carbon support oxidation rates (i.e. lower rates of CO₂ formation) for shutdowns than for startups.

- We used GDLs and catalyst layers with relatively high permeability and porosity, and 90% humid gases. Shutdowns may be more damaging than startups in some other scenarios: higher degradation during shutdowns have been recorded under various conditions and relatively long residence time compared with startup [24,25]. Ishigami et al. [25] visualized in situ spatial distribution of O₂ across the cell area during SU and SD. While the nominal O₂/H₂ residence times were the same during SU and SD ($\approx 1 \text{ s}$), the actual times to completely exchange the gases on the anode side were 2 s for SU, and 6 s for SD. Longer gas replacement time during shutdown can be attributed to slower diffusion of O₂ compared to H₂, as well as to O₂ consumption to form water. The difference in gas replacement times (or, the effective residence times) between SU and SD became smaller as the cells degraded during repeated SU and SD cycling. Thus, according to the results of Ishigami et al. [25], mass transport can be the dominating factor for the relative effects of startup vs. shutdown in our case.
- Depending on the flow field (land/channel ratio) and MEA structure (GDL and catalyst layer thickness and porosity), one can expect two types of in-plane variations for carbon corrosion rates: (1) inlet vs. outlet (carbon corrosion variation along the channel length, governed by inlet-outlet internal currents), and (2) land vs. channel region (variation in the direction perpendicular to the channel). Internal currents between channel and land regions were measured recently by Schneider et al. [12], while the land/channel variations in degradation levels were studied by Durst et al. [19]. Slower gas transport under the lands effectively increases local residence time and promotes carbon corrosion leading to non-uniform in-plane degradation. This situation may be anticipated in certain flow-field designs (e.g. when the lands are very wide) and/or when the porosity (or, permeability) of GDLs and catalyst layers is low. Such mass transport induced effects may also alter the relative degradation levels between SU and SD.

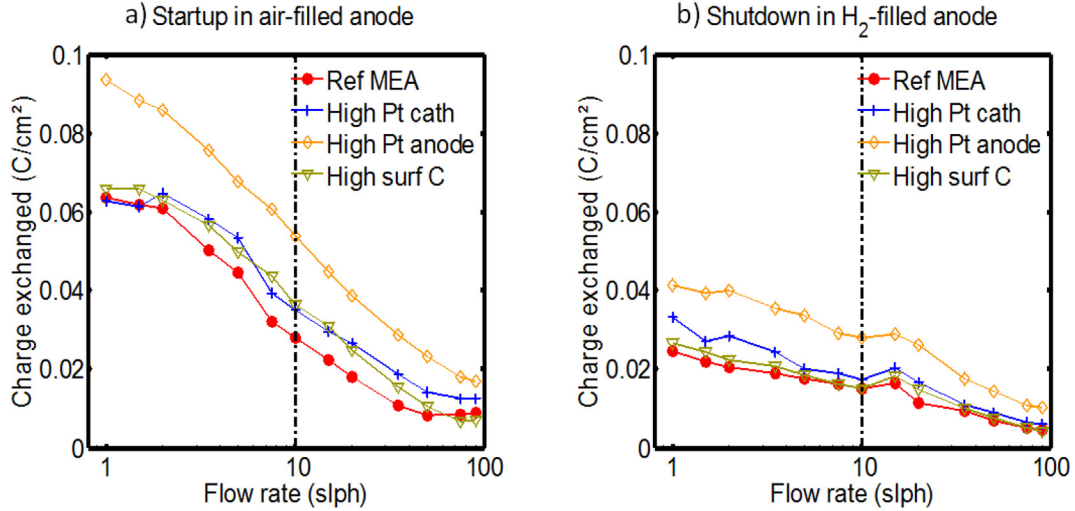


Fig. 4. Effect of the MEA material and the gas flow rate on the charge exchanged between the active and passive parts of the fuel cell (reverse currents integrated over the entire cell area and divided by the cell active area [9]) during single startups (a) and shutdowns (b).

Apart from slight variations in the maximum values, the trends in time evolution of the internal currents were similar with the four tested MEAs. To better distinguish between different MEAs, the charge transferred from the active to the passive regions of the cell is plotted as a function of the gas injection flow rate (Fig. 4). In both SU and SD cases, the total charge exchanged decreased when the hydrogen or air flow rates increased (i.e. the charge decreases with decreasing residence time). Further, the total charge exchanged is lower during shutdowns, indicating lower degradation, as discussed in the preceding paragraphs. Only the MEA with a higher anode Pt loading differed significantly from the other three MEAs, with more charge exchanged. In contrast, increasing the cathode Pt loading ($2\times$) or the carbon specific surface area ($3\times$), Table 1, does not result in any noticeable change in the charge exchanged. Thus the anode appears to be the limiting electrode for the reverse current (for the present cell design, materials, and conditions), which is not surprising considering that the main reaction in the passive region of the cell is oxygen reduction (Fig. 1). This conclusion applies to startups as well as to shutdowns.

Fig. 5 depicts the CO₂ evolution (in term of carbon loss) during SU and SD, as a function of the hydrogen or air injection flow rates. Like the charge exchanged, the CO₂ emissions decrease with the gas

flow rate, which confirms the link between carbon corrosion and reverse currents observed by Reiser et al. [6]. Lower CO₂ emissions measured during shutdowns are in agreement with the results of Gu et al. [15], Kreitmeier et al. [20], Shen et al. [14], as well as with our recent work [10,19]. Different MEAs show more distinction in the CO₂ evolution compared to that of the charge exchanged (Fig. 4): the CO₂ emissions were 30–50% higher with the high surface carbon ($800\text{ m}^2/\text{g}$ amorphous carbon) than with the reference electrode ($240\text{ m}^2/\text{g}$ Vulcan XC72). Second, a higher anode Pt loading ($0.18\text{ mg}_{\text{Pt}}/\text{cm}^2$ against $0.08\text{ mg}_{\text{Pt}}/\text{cm}^2$ with the reference MEA) yields about 50% higher CO₂ formation. In contrast, increasing the Pt loading at the cathode ($0.44\text{ mg}_{\text{Pt}}/\text{cm}^2$ vs. $0.2\text{ mg}_{\text{Pt}}/\text{cm}^2$ with the reference MEA) significantly limits the CO₂ emissions. The main observations from these results are summarized as follows.

- The increase of CO₂ emissions with the anode Pt loading suggests that the anode electrode governs the reverse currents and thus the carbon corrosion at the cathode. During startups, a higher anode Pt loading favors ORR in the passive part of the anode compartment, and consequently promotes carbon corrosion in the passive part of the cathode compartment (Fig. 1). Thus, one possible avenue for reducing the carbon

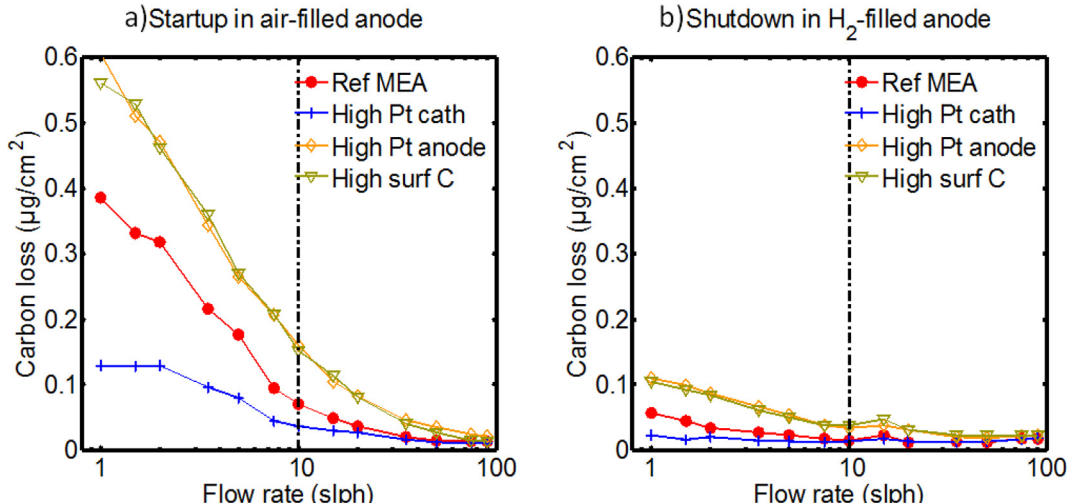


Fig. 5. Carbon loss due to CO₂ emissions per (single) startup (a) and shutdown (b) vs. gas flow rate.

corrosion is by lowering the Pt loading in the anode catalyst layer: oxygen reduction in the passive part of the anode seems to be the limiting phenomenon for both the reverse current and carbon oxidation. This methodology is similar but different as in other project where the ORR activity is limited by using Pt–Ru electrocatalysts [27].

- Amorphous carbon with a high specific surface was more sensitive to corrosion, especially during startups. The CO₂ emissions were about 50% above those measured with the reference MEA for the lowest hydrogen injection flow rate (1 slph) as well as with 10 slph (this flow rate was used for the aging protocols presented in Section 4). The same tendency is observed for shutdowns.
- Increase of the cathode Pt loading resulted in a slight augmentation of the charge exchanged (Fig. 4), however, it also entailed a significant decrease of the CO₂ emissions (Fig. 5). Although the similar shape of the curves in Figs. 4 and 5 indicates a strong correlation between the reverse currents and carbon corrosion, their response to a change in the MEA specification differ. The main reason is that the charge due to CO₂ emissions presents only a small contribution to the charge measured from the reverse currents. Relative contribution of the CO₂ charge to the total charge measured is plotted in Fig. 6. For example, the MEA with high specific surface area carbon at the cathode releases 0.60 µg cm⁻² of CO₂ during startup with 1 slph H₂ (Fig. 5, left). This corresponds to 0.02 C cm⁻², or about 30–35% of the total charge exchanged measured from the internal currents (this is also the maximum contribution, Fig. 6). For the same H₂ flow rate, the CO₂ emissions contribution to the charge exchanged is only 7% using the MEA with high cathode Pt loading. Since the capacitive contribution to the reverse current is also relatively low (it can be roughly evaluated to about 0.004 C cm⁻² by considering a double layer capacity of about 0.004 F cm⁻² on the anode side and a voltage variation of 1 V during both SU and SD), we can conclude that up to 80% of the reverse current is still not quantified with the present setup. This current is probably linked to reversible phenomena such as partial carbon oxidation, reversible Pt oxidation, and water splitting. For the MEA with increased cathode Pt loading, these mechanisms absorb a higher portion of charge transfer during SU and SD, likely keeping potential lower and thus limiting strongly complete carbon oxidation.

4. Aging protocols for startup and shutdown

Two different aging protocols, one for startup and the other for shutdown, were employed to distinguish between the SU and SD effects on degradation rates and performance losses (Fig. 7). The gas (H₂ for startup and air for shutdown) inlet flow rate on the anode was set to 10 slph for both SU and SD, with 90% RH for all gases at all times. In the startup aging protocol, hydrogen is introduced in the air-filled anode compartment, whereas the shutdown effects were minimized by injecting high flow of nitrogen during each shutdown (instead of using air). In the shutdown aging protocol, air was introduced in the hydrogen-filled anode compartment, whereas the fuel cell was started-up again only after carefully flushing the anode compartment with nitrogen, which minimized the startup effects (i.e. the startups were performed by injecting H₂ into N₂-filled anode). In both the SU and SD aging protocol, fuel cell was operated at a fixed current density of 0.67 A cm⁻² for 5 min between two consecutive SU/SD sequences in order to monitor the performance decrease. The aging protocols were interrupted periodically after 30 SU/SD sequences to measure the ElectroChemical Surface Area (ECSA) in 100% RH H₂/N₂. The charge exchanged and the CO₂ evolution were also measured every 30 SU/SD sequences.

The aging protocol was stopped once the ECSA had decreased by about 50% (40% in the case of the MEA with a higher Pt loading at the cathode).

4.1. Global effect of SU and SD aging on the cell performance, CO₂ evolution, and ECSA

Fig. 8 shows the performance degradation with aging time for the four MEA materials, i.e. the decay of the cell voltage at fixed current as a function of the number of SU or SD sequences. The SU/SD data show that the startups cause more severe and faster performance degradation than the shutdowns, regardless of the MEA material. At the beginning of life (BoL), the voltage with the MEA with high carbon surface was the lowest, although increasing the carbon specific surface area, as well as the Pt loading on cathode or anode, generally improves slightly the fuel cell performance. In the present case, the effect of an increase of Pt loading on anode and cathode is relatively high, which is not surprising considering that the fuel cell is operated at atmospheric pressure and the ECSA

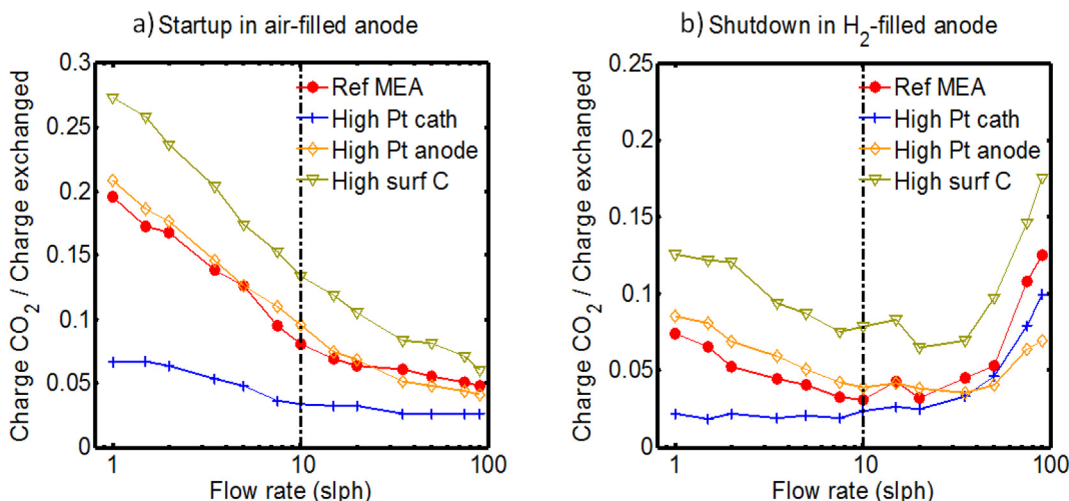


Fig. 6. Relative contribution of charge from CO₂ emissions to the total charge exchanged per startup (a) and shutdown (b) vs. gas injection flow rate. The increase of the CO₂/charge exchanged ratio with the air injection flow rate at shutdown (right plot) may not be significant considering that the measured values are extremely low.

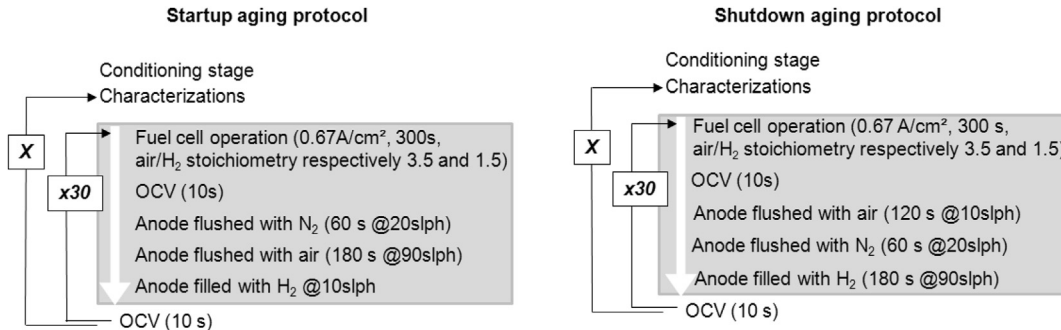


Fig. 7. Startup and shutdown aging protocol. The main sequence (X) was repeated between 10 and 25 times – depending on the tested materials – to reach 50% ECSA loss, which corresponds to 390–750 startups or shutdowns.

numbers given in Table 1. The MEAs with high anode Pt loading and high cathode carbon support surface area exhibited the fastest performance decay. This behavior is consistent with the highest CO₂ emissions measured with these MEAs. The best performance as well as the best durability was obtained with the MEA having a higher Pt loading at the cathode. This result is consistent with the lowest CO₂ emissions measured with this MEA (Fig. 9), which remained lower than with the other MEAs over the entire duration of the aging protocols. All MEAs show rapid decrease of the CO₂ emission during the first 30–60 cycles, followed by a slower decrease in CO₂ formation during the next 200 or 300 cycles. The CO₂ evolved during individual startups or shutdowns remains constant thereafter. The rapid initial decrease in the CO₂ evolution can be linked to the combined effects of the ECSA decrease (carbon corrosion, Pt agglomeration and migration), the increase of the graphitized-to-amorphous carbon ratio, and to the progressive passivation of carbon because of partial oxidation. In addition, new electrodes may contain less anchored or less stable carbon particles, which are thus more prone to oxidation.

Finally, Fig. 10 presents the decrease of the ECSA (expressed in m²_{Pt}/m²_{MEA}) to facilitate comparison between different MEAs) as a function of the number of SU or SD cycles. As expected, the ECSA decreased at a slightly but consistently faster rate during the SU aging protocols and there were several notable differences between the MEAs (as summarized in Table 2). At the onset of SU and SD aging protocols (during the first 90 cycles), the MEA with a high

anode Pt loading showed the fastest ECSA decrease, which is consistent with the previous observations regarding the charge exchanged (Fig. 4) and CO₂ emissions (Figs. 5 and 9). The ECSA drop was slower for the reference MEA, and the slowest for the MEA with high cathode Pt loading, which is also consistent with the previous results. However, the initial ECSA rate of decrease of the MEA with high surface area carbon at the cathode was equivalent (for SD) or slightly lower (for SU) than that of the reference MEA, although the charge exchanged were slightly higher (Fig. 4 – gas injection flow rate of 10 slph) and CO₂ emissions (Figs. 5 and 9) were significantly higher (for SU and SD). The ECSA degradation rates are different after 300 SU or SD cycles. The ECSA degradation of the MEA with the high specific area carbon cathode becomes almost identical to that observed with the reference MEA. The high cathode Pt loading still offers efficient protection against ECSA decay while high anode Pt loading has the opposite effect. After 300 cycles, the ECSA with high cathode Pt loading MEA degrades roughly 50% slower than the remaining three MEAs, which ECSAs degrade at similar rates.

According to Fig. 9, using high specific surface area carbon at the cathode yields CO₂ emissions 50–100% higher than with the reference MEA while having lower or similar ECSA decrease rates (Table 2). These results suggest that carbon corrosion may have a limited impact on the ECSA decrease depending on the cathode carbon support and Pt loading. Compared to the reference MEA, high surface area carbon support tends to have better dispersed Pt particles (i.e. further apart from each other). We can hypothesize

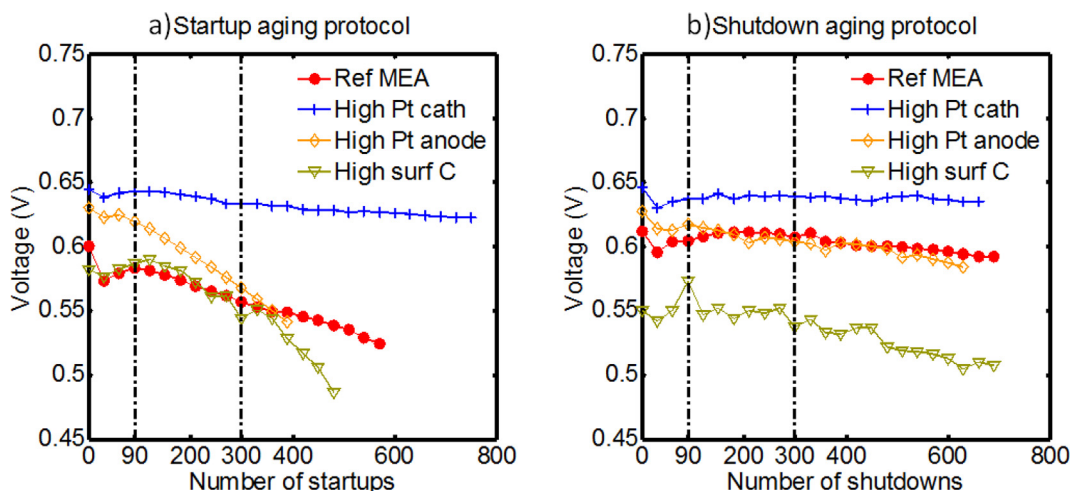


Fig. 8. Time evolution of the cell voltage at fixed current density 0.67 A cm⁻² during SU and SD aging protocols with four different MEA materials. The vertical lines at 90 and 300 cycles correspond to comparison points in Tables 2 and 3. (a) Startup aging protocol. (b) Shutdown aging protocol. It must be noted that except for the MEA with high surface carbon, carbon corrosion during shutdown is not significant enough to entail strong voltage decrease at 0.67 A cm⁻².

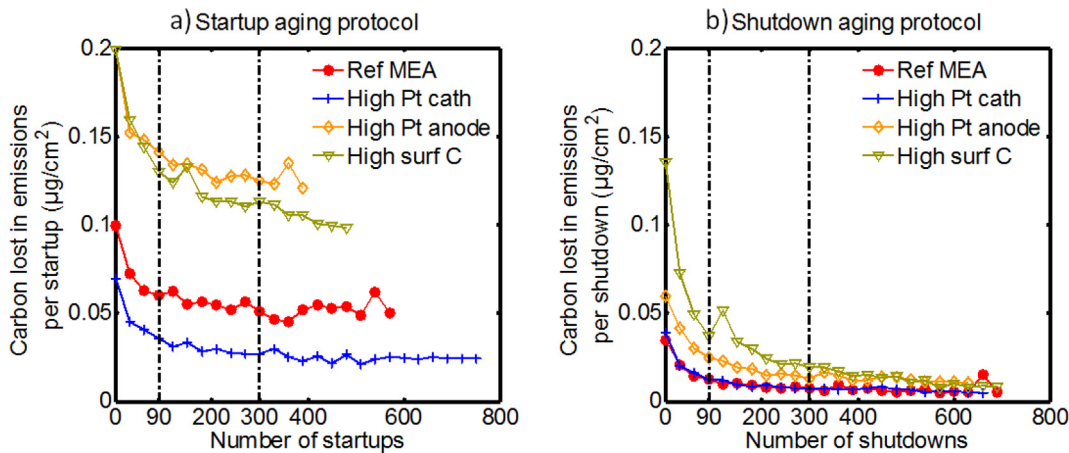


Fig. 9. Time evolution of carbon loss due to CO_2 emissions (per cycle) during SU and SD aging protocols with four different MEA materials. The vertical lines at 90 and 300 cycles correspond to comparison points in Tables 2 and 3. (a) Startup aging protocol. (b) Shutdown aging protocol.

that such initial electrode structure may offset the ECSA decrease, while having more amorphous carbon surface available for corrosion. At the same time, severe carbon corrosion causes a substantial drop in the performance that may be attributed to the reduction in the electrode porosity and collapse of the porous structure, albeit that the ECSA degrades at a similar rate as with the reference MEA. Thus, while the corrosion of the carbon support ultimately promotes the ECSA decrease, the initial ECSA drop with the reference MEA appears to be caused mostly by the short-range Ostwald ripening, long-range Ostwald ripening, or Pt migration/coalescence. Our results even suggest that at the beginning of the SU aging protocol, carbon corrosion limits the ECSA decrease. According to Table 3 and Fig. 8, high specific surface carbon had a dramatic impact on the degradation of the cell performance, most likely because of structural changes in the electrodes at the micro-scale, similar to those evidenced by Dubau et al. [17] and Gasteiger et al. [18]. Carter et al. showed recently that 10% wt. of carbon loss was enough to severely damage the electrode porosity [28]. In our case, $0.1\text{--}0.2 \mu\text{g cm}^{-2}$ /SU carbon loss measured from the CO_2 emissions (Fig. 9, MEA with high specific surface carbon at the cathode) corresponds to a total loss of about $0.03\text{--}0.06 \text{ mg cm}^{-2}$ after 300 SU, or 8–16% of the initial mass of carbon at the cathode (about 0.4 mg cm^{-2}). The impact of ECSA losses on fuel cell voltage

(at 0.67 A cm^{-2}), summarized in the last two columns of Table 3, can vary substantially (from 0 to $2560 \mu\text{V cm}^{-2}\text{Pt}/\text{cm}^2\text{MEA}$) depending on the aging protocol (SU or SD) and the MEA specification.

4.2. Effect of SU and SD aging on local degradation along the gas channels

Fig. 11 shows the local ECSA decrease measured along the gas channels during startup and shutdown aging protocols performed with the reference MEA. 570 SU and 690 SD were necessary to lose about 50% of the initial value of the average ECSA. The segments suffering the most degradation were located close to the anode outlet (segment #1, Fig. 2) during startups and close to the anode inlet (segments #17 and #18, Fig. 2) during shutdowns. As expected, since these regions of the cell are subjected to the air/air condition for prolonged times, they also exhibited the most severe ECSA degradation.

Similar results were obtained using MEA with high Pt loading at the anode and with high specific surface area carbon at the cathode. The only difference was the duration of the aging protocols needed to achieve 50% ECSA loss: 390 SU or 630 SD for high anode Pt loading MEA, and 510 SU or 690 SD for the high specific surface area

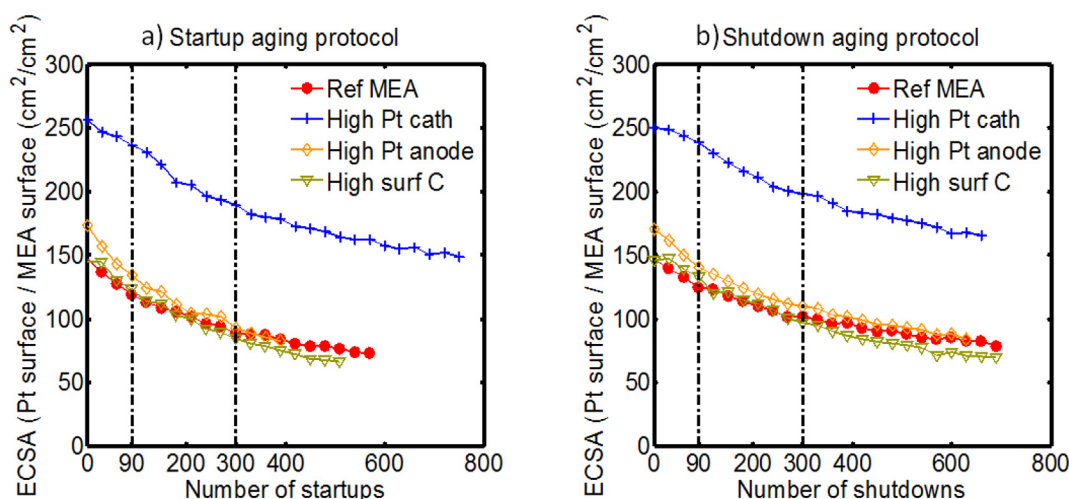


Fig. 10. Time evolution of the ECSA during SU and SD aging protocols with four different MEA materials. The vertical lines at 90 and 300 cycles correspond to comparison points in Tables 2 and 3. (a) Startup aging protocol. (b) Shutdown aging protocol.

Table 2

Cumulative ECSA decrease after 90 and 300 startups and shutdowns for the four tested MEAs. ECSA at BoL is given in [Table 1](#).

MEA	ECSA decrease after 90 cycles ($\text{cm}^2 \text{Pt}/\text{cm}^2 \text{MEA}$)		ECSA decrease after 300 cycles ($\text{cm}^2 \text{Pt}/\text{cm}^2 \text{MEA}$)	
	Startup	Shutdown	Startup	Shutdown
Reference MEA	-14	-11	-30	-23
Higher cathode Pt loading	-5	-3	-17	-13
Higher anode Pt loading	-17	-13	-35	-26
Higher carbon specific surface	-11	-7	-30	-25

carbon MEA. However, the MEA with high cathode Pt loading showed a different behavior. Not surprisingly, the time required to reach a significant ECSA loss was longer than with the other MEAs (750 SU and 660 SD for a 40% drop). Because of the lower charge exchanged between the active and passive regions of the cell with this MEA ([Fig. 4](#)), the ECSA drop spatial distribution was also much more homogenous along the cell. The final difference in the average ECSA decrease (after 750 cycles) between the anode outlet region (segments 1–5) and the anode inlet region (segments 15–20) was less than 6% points (e.g. 31% vs. 37% ECSA decrease after complete SD protocol for anode outlet vs. inlet, respectively, and 43% vs. 40% after complete SU protocol). For comparison, the reference MEA showed larger variations in ECSA decrease between the anode inlet and outlet regions (e.g. 14% point after complete SD protocol cycles and 13% points after complete SU protocol, [Table 4](#)) for a similar average ECSA loss (50%).

The impact of this spatially non-uniform ECSA degradation on local performance is observed through the time evolution of the local polarization curves, shown in [Fig. 12](#) for startups (top) and shutdowns (bottom) with reference MEA. The performance decrease was more pronounced in the regions exposed longest to air in the anode compartment. The largest local decay in the performance is exhibited in the anode outlet region (segment #1) after prolonged SU cycling ([Fig. 12](#), top left), in agreement with the local ECSA loss ([Fig. 11](#), left). After prolonged SD cycling, local performance loss is largest at the anode inlet ([Fig. 12](#), bottom right). This local degradation in the performance is in agreement with the results discussed earlier in the text, where the SD aging protocol is less damaging than the SU aging at the cell level. The local performance drop caused by the SD protocol is illustrated by the polarization curves of segments #17 in [Fig. 12](#). The local ECSA degradation ([Fig. 11](#)) for SD was most severe in this segment, rather than at the anode inlet itself (segment #20). This spatial shift of the highest ECSA loss after SD protocol is likely caused by some local flow mal-distributions due to the proximity of the inlet manifold.

Table 3

Average voltage drop per (individual) SU or SD during the first 300 cycles and voltage drop per ECSA loss.

MEA	Average voltage loss (300 SU) ($\mu\text{V}/\text{SU}$)	Average voltage loss (300 SD) ($\mu\text{V}/\text{SD}$)	$\Delta V/\Delta_{\text{ECSA}}$ (300 SU) ($\mu\text{V cm}^{-2} \text{Pt}/\text{cm}^2 \text{MEA}$)	$\Delta V/\Delta_{\text{ECSA}}$ (300 SD) ($\mu\text{V cm}^{-2} \text{Pt}/\text{cm}^2 \text{MEA}$)
Reference MEA	-124	-50	1240	652
Higher cathode Pt loading	-47	Not significant	829	Not significant
Higher anode Pt loading	-238	-63	2040	727
Higher carbon specific surface	-256	-42	2560	504

Nevertheless, the performance decrease in segment #20 was noticeable.

5. Reproducibility and uncertainty of the experimental results

The reproducibility of the results was assessed by repeating the measurements of the CO₂ emissions and charge exchanged with four sets of new materials (reference MEAs and GDLs). The testing protocol was identical to that described in Section 3, while the results are summarized in [Fig. 13](#). The aging protocols (Section 4) were performed with air and hydrogen injection flow rates set to 10 slph. For this value, the dispersion of the charge exchanged is of the order of $\pm 4\%$ for SU and $\pm 8\%$ for SD, while that of the evolved CO₂ (expressed in term of carbon emissions) is of the order of $\pm 6\%$ for SU and $\pm 17\%$ for SD, which is sufficiently low, confirming that the variations discussed in Sections 3 and 4 are significant. Furthermore, [Fig. 13](#) shows that the dispersion tends to decrease when the gas injection flow rates increase, while both the charge exchanged and CO₂ emissions are also lower at high flow rates. This indicates that the higher dispersion observed for the lowest injection flow rates is probably due to physical phenomena and/or variations in the material properties rather than to the experimental setup. With the set of 4 new MEAs used in [Fig. 13](#), we measured average ECSA of $64.5 \pm 1.5 \text{ m}^2/\text{g}_{\text{Pt}}$, permeation current density of $1.6 \pm 0.4 \text{ mA cm}^{-2}$, and voltage at 0.67 A cm^{-2} of $0.614 \pm 0.015 \text{ V}$. These values were measured at BoL, right after the conditioning stage.

Finally, the accuracy of charge measurements was also assessed by considering the charge exchanged between the active and passive parts of the cell as a function of the number of segments along the cell. The charge was measured with varying level of segmentation: by removing the electrical insulation between the adjacent segments ([Fig. 2](#)), the cell was divided into 2, 4, 5, 10, and 20 segments. The total length of the channels is 30 cm. [Fig. 14](#) shows that there is a threshold value (10 segments, each 3 cm in length) below which the charge exchanged is clearly underestimated by lumping the internal currents between the individual 1.5 cm long segments. According to these results, dividing the cell into 10 segments instead of 20 leads to an additional measurement error lower than 1% (for this 10 slph flow). However, there may be internal currents between the electrode regions under the channels and under the lands [12]. These internal currents, accompanied by the longer mixing or residence times under the lands, may cause degradation heterogeneities in the cathode catalyst layer under the lands (more degradation) and under the channels (less degradation) [20]. Such issues were not considered in this work.

6. Conclusions

Separate testing protocols for fuel cell startup (SU) and shutdown (SD) were developed to distinguish between the effects of SU and SD on performance degradation. The internal currents during SU and SD operation were measured in a segmented cell to evaluate the charge exchanged between the active (H₂/Air) and passive (Air/Air) portions of the cell. Carbon corrosion was quantified by measuring the CO₂ emissions at the cathode exhaust. The influence of flow rates, H₂ for startup and air for shutdown, was investigated during individual SUs and SDs. Spatial degradation of the cell was characterized periodically during repeated SU and SD cycling, by measuring the local Electro Chemical Surface Area (ECSA) as well as local polarization curves. The cathode Pt loading, anode Pt loading and the type of cathode carbon support were examined to determine their effects on spatially resolved ECSA and performance degradation.

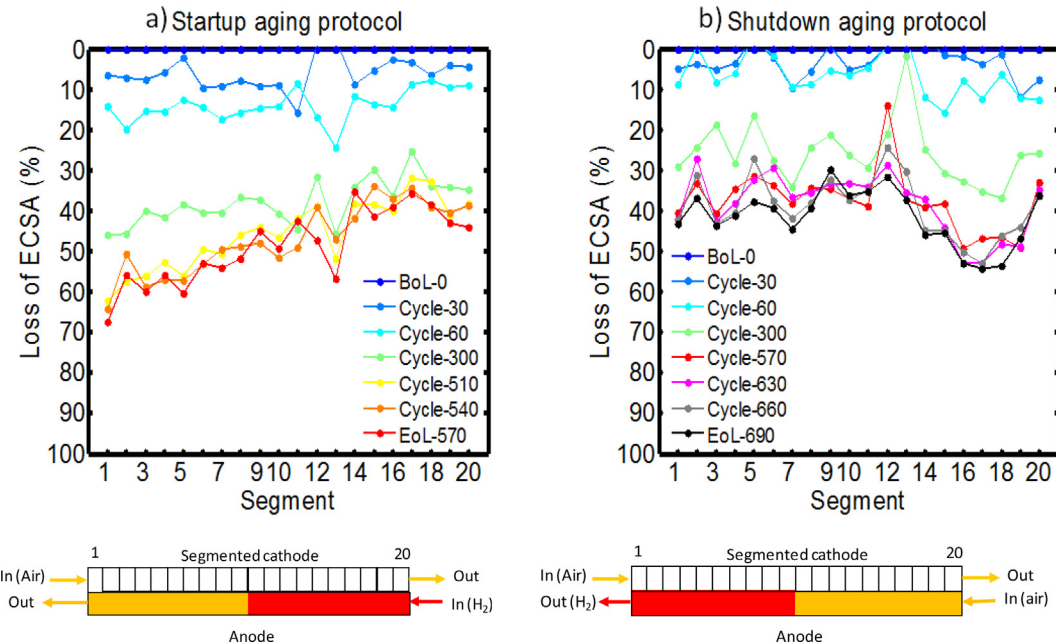


Fig. 11. Top: time evolution of local ECSA along the cell length during startup (a) and shutdown (b) aging protocols for the reference MEA. Bottom: schematic of the gas flow in the anode compartment during startup (a) and shutdown (b).

Table 4

Comparison of %ECSA drop at anode inlet and outlet over the whole aging protocols. The startup and the shutdown protocols were performed separately with fresh MEAs and they were stopped once the average ECSA had decreased by about 50% (40% in the case of the MEA with a higher Pt loading at the cathode).

MEA	%ECSA drop at anode outlet over the whole aging protocols (average values segment 1–5)				%ECSA drop at anode inlet over the whole aging protocols (average values segment 15–20)			
	Startup		Shutdown		Startup		Shutdown	
	Segment	Value	Segment	Value	Segment	Value	Segment	Value
Reference MEA (570 SU or 690 SD)	58		40		44		54	
Higher cathode Pt loading (750 SU or 690 SD)	43		31		40		37	
Higher anode Pt loading (390 SU or 630 SD)	62		46		31		56	
Higher carbon specific surface (510 SU or 690 SD)	69		40		38		60	

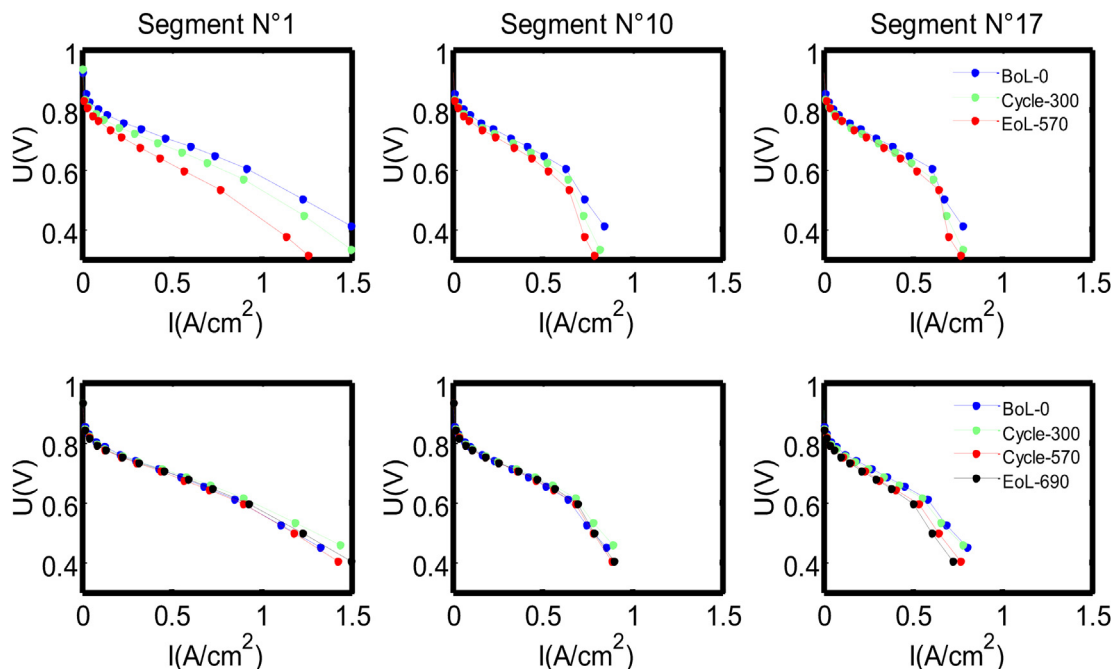


Fig. 12. Time evolution of local polarizations curves for individual segments during startup and shutdown aging protocols with the reference MEA. Segment #1 = anode outlet, Segment #20 = anode inlet. Top: SU aging protocol. Bottom: SD aging protocol. The corresponding spatial distributions of the ECSA degradation levels over time are shown in Fig. 10.

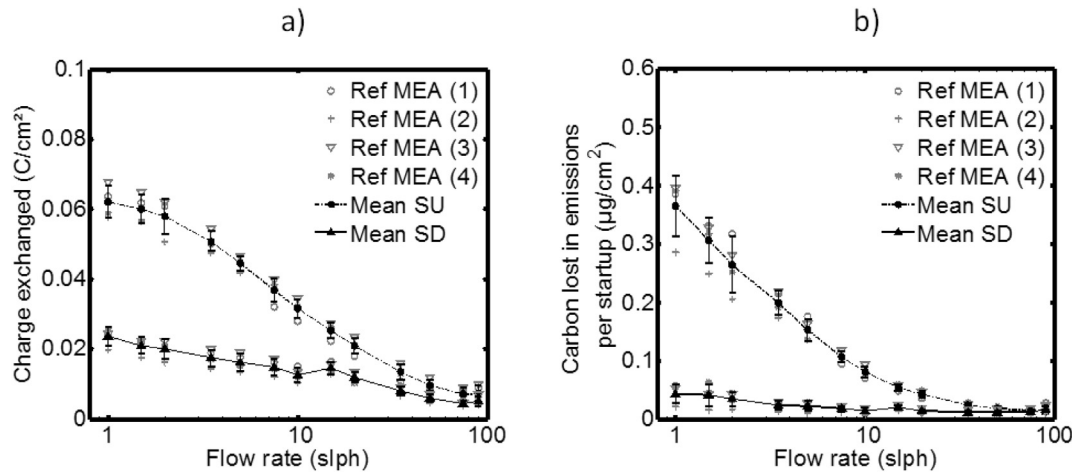


Fig. 13. Reproducibility tests carried out with four different samples of the reference MEA. Charge exchanged (left plot) and carbon emission (right plot) vs. gas flow rate (H_2 for SU, air for SD). Variation of the charge exchanged: $\pm 0.002 \text{ C cm}^{-2}$ average and $\pm 0.003 \text{ C cm}^{-2}$ maximum. Variation of the carbon emissions: $\pm 0.005 \mu\text{g cm}^{-2}$ average and $\pm 0.025 \mu\text{g cm}^{-2}$ maximum.

During startups and shutdowns, the charge exchanged between the active and passive regions of a fuel cell is a function of the common residence time of air and hydrogen in the anode compartment. Both the CO_2 emissions and the charges exchanged increase with the residence time. However, the complete oxidation of carbon to CO_2 accounts for only a portion (no more than 25%) of the reverse currents. The remaining contributions to the total charge measured from internal currents come from a combination of partial oxidation of carbon, water splitting and reversible/irreversible platinum oxidation.

For equivalent nominal gas residence times, startups are more damaging than the shutdowns in present experiments, regardless of the MEA type, i.e. regardless of the catalyst loading on anode and cathode, or carbon support surface area at the cathode. This is explained by Pt oxidation in the passive part of the anode compartment once air is introduced at SD, which lowers the reverse currents and thus carbon support corrosion rates on the

cathode. Higher degradation during startups is corroborated by more CO_2 evolution and more severe ECSA decrease.

Prolonged SU and SD protocols cause non-uniform ECSA loss and performance degradation along the cell geometry. The performance decrease is more pronounced in the local regions exposed to air in the anode compartment the longest (i.e. regions of the cell that are in the passive, air/air mode, for prolonged time periods during each startup or shutdown). The largest local decay in the performance is exhibited in the anode outlet region after prolonged SU cycling. After prolonged SD cycling, local performance loss is largest at the anode inlet. Spatial variation is substantially lower after SD than after SU protocol, in agreement with the overall less degradation caused by the SD protocol.

The decrease in the fuel cell performance and ECSA is also quite sensitive to the MEA specifications: anode and cathode catalyst loading, and type of cathode carbon support. The results indicate that the degradation induced by startup and shutdown may be mitigated by tuning the MEA specifications. One possible avenue for reducing the carbon corrosion is to lower the Pt loading in the anode catalyst layer to limit the oxygen reduction in the passive part of the anode. Not surprisingly, higher cathode loading shows more durable performance, but also shows more uniform degradation as opposed to lower loadings which have non-uniform degradation. High surface area carbon support exhibits substantially higher rates of CO_2 evolution than the reference MEA while having an ECSA degradation rate much closer to the baseline case. Based on this observation, one could propose that the abundant amount of amorphous (or, easily oxidized) carbon surfaces may serve as sacrificial carbon, which could offset the ECSA loss at the onset of the aging protocol.

Detailed ex situ characterization of the tested MEA materials is ongoing and will be presented in a separate publication. In addition, a numerical model under development will consider the governing electrochemical reactions occurring in the active and passive regions of the cell, as well as mass transport limitations.

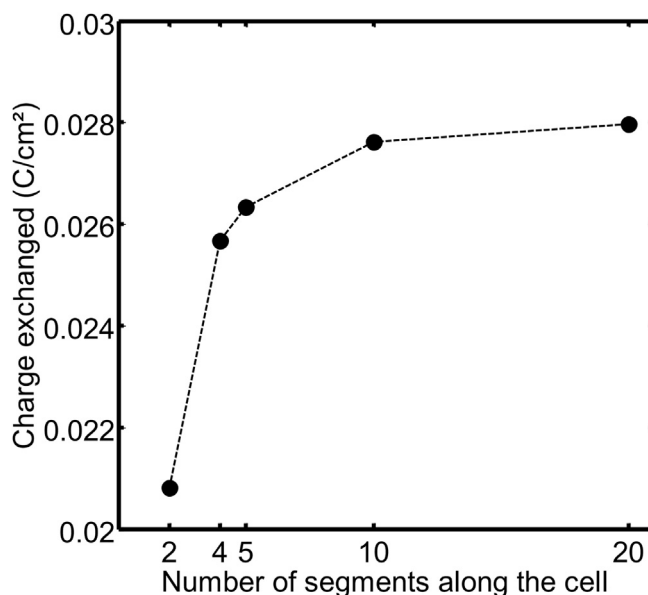


Fig. 14. Charge exchanged vs. the number of electrically insulated segments along the cell. Data shown are for the startup with 10 slph of hydrogen introduced in air-filled anode, with the reference MEA.

Acknowledgments

Members of the group from Los Alamos National Laboratory wish to acknowledge the funding from the US Department of Energy, the Office of Energy Efficiency and Renewable Energy, Fuel Cell Technologies Office, and the support of the technology

development manager Nancy Garland. We also acknowledge SGL Carbon GmbH for supplying the GDL materials, and Ion Power for fabricating the MEAs. We thank Greg James and Mark Watson of Ballard Power Systems for useful discussions regarding the development of startup/shutdown protocols.

Members of the group from Lorraine University and CNRS wish to acknowledge the funding from Région Lorraine and CNRS.

References

- [1] R. Borup, J. Meyers, B. Pivovar, Y.S. Kim, R. Mukundan, N. Garland, et al., *Chem. Rev.* 107 (2007) 3904.
- [2] L. Flandin, A.S. Danérol, C. Bas, E. Claude, G. De-Moor, N. Albérola, *J. Electrochem. Soc.* 156 (2009) B1117.
- [3] E. Guilmot, A. Corcella, M. Chatenet, F. Maillard, F. Charlot, G. Berthomé, C. Iojoiu, J.-Y. Sanchez, E. Rossinot, E. Claude, *J. Electrochem. Soc.* 154 (2007) B1106.
- [4] D. Spernjak, J.D. Fairweather, T. Rockward, R. Mukundan, R.L. Borup, *J. Power Sources* 214 (2012) 386–398.
- [5] J.D. Fairweather, D. Spernjak, R. Mukundan, R. Ahluwalia, S. Arisetty, R.L. Borup, *ECS Trans.* 50 (2) (2013) 1589–1597.
- [6] C.A. Reiser, L. Bregoli, T.W. Patterson, J.S. Yi, J.D. Yang, M.L. Perry, T.D. Jarvis, *Electrochem. Solid State Lett.* 8 (6) (2005) A273–A276.
- [7] M.L. Perry, T. Patterson, C. Reiser, *ECS Trans.* 3 (2006) 783–795.
- [8] Y. Yu, H. Li, H. Wang, Y. Xiao-Zi, G. Wang, M. Pan, *J. Power Sources* 205 (2012) 10–23.
- [9] A. Lamibrac, G. Maranzana, O. Lottin, J. Dillet, J. Mainka, S. Didierjean, A. Thomas, C. Moyne, *J. Power Sources* 196 (2011) 9451.
- [10] J. Dillet, A. Lamibrac, G. Maranzana, J. Durst, D. Spernjak, J. Fairweather, R. Mukundan, R.L. Borup, S. Didierjean, O. Lottin, *ECS Trans.* 50 (2) (2013) 701–710.
- [11] G. Maranzana, C. Moyne, J. Dillet, S. Didierjean, O. Lottin, *J. Power Sources* 195 (2010) 5990.
- [12] A. Schneider, S. von Dahlen, *Electrochem. Solid State Lett.* 14 (2) (2011) B30–B33.
- [13] S. Didierjean, A. Lamibrac, T. Geneston, A. Rakotondrainibe, G. Maranzana, E. Rozier, F. Beille, O. Lottin, *Int. J. Hydrogen Energy* 37 (2012) 6798–6807.
- [14] Q. Shen, M. Hou, D. Liang, Z. Zhou, X. Li, Z. Shao, B. Yi, *J. Power Sources* 189 (2) (2009) 1114–1119.
- [15] W. Gu, R.N. Carter, P.T. Yu, H.A. Gasteiger, *ECS Trans.* 11 (2007) 963–973.
- [16] N. Linse, L. Lorenz, G.G. Scherer, A. Wokaun, *Electrochim. Acta* 56 (2011) 7541–7549.
- [17] L. Dubau, J. Durst, F. Maillard, M. Chatenet, J. André, E. Rossinot, *Fuel Cells* 12 (2012) 188–198.
- [18] H.A. Gasteiger, D.R. Baker, R.N. Carter, W. Gu, Y. Liu, F.T. Wagner, P.T. Yu, in: D. Stolten (Ed.), *Hydrogen Energy*, WILEY-VCH – Verlag GmbH & Co, 2010, p. 3.
- [19] J. Durst, A. Lamibrac, F. Charlot, J. Dillet, L.F. Castanheira, G. Maranzana, L. Dubau, F. Maillard, M. Chatenet, O. Lottin, *Appl. Catal. B: Environ.* 138–139 (2013) 416–426.
- [20] S. Kreitmeier, A. Wokaun, F.N. Büchi, *J. Electrochem. Soc.* 159 (11) (2012) F787–F793.
- [21] A. Lamibrac, Ph. D. dissertation, Université de Lorraine, pp. 66–72 and 76–78 (2013).
- [22] N. Linse, G.G. Scherer, A. Wokaun, L. Gubler, *J. Power Sources* 219 (2012) 240–248.
- [23] J.H. Kim, Y.Y. Jo, E.A. Cho, J.H. Jang, H.J. Kim, T.H. Lim, I.H. Oh, J.J. Ko, I.J. Son, *J. Electrochem. Soc.* 157 (2010) B633.
- [24] A.B. Ofstad, J.R. Davey, S. Sunde, R.L. Borup, *ECS Trans.* 16 (2008) 1301.
- [25] Y. Ishigami, K. Takada, H. Yano, J. Inukai, M. Uchida, Y. Nagumo, T. Hyakutake, H. Nishide, M. Watanabe, *J. Power Sources* 196 (6) (2011) 3003–3008.
- [26] W. Gu, P.T. Yu, R.N. Carter, R. Makharia, H.A. Gasteiger, *Modeling and Diagnostics of Polymer Electrolyte Fuel Cells*, Modern Aspects of Electrochemistry, 49, Springer Science & Business Media LLC, 2010, p. 45.
- [27] R. Atanasoski, Doe Fuel Cell Technologies Office 2013 – Annual Merit Review Proceedings (2013).
- [28] R.N. Carter, W.B. Gu, B. Brady, P.T. Yu, K. Subramanian, H.A. Gasteiger, in: W. Vielstich, H.A. Gasteiger, H. Yokokawa (Eds.), *Handbook of Fuel Cells: Fundamentals, Technology and Applications*, vol. 6, John Wiley & Sons, Chichester, 2009, p. 829.